Theoretical and experimental evaluation of thermal interface materials and other influencing parameters for thermoelectric generator system

Krishnadass Karthick [a, c], S Suresh [a]*, Harjit Singh [b], Grashin C Joy [a], R Dhanuskodi [c]

[a] Department of Mechanical Engineering, National Institute of Technology, Tiruchirappalli, India.

Email: karthick@bhel.in, grashincjoy@gmail.com

Email: *Corresponding author: ssuresh@nitt.edu

[b] College of Engineering, Design and Physical Sciences, Brunel University London, Uxbridge, UB8 3PH, UK.

Email: harjit.singh@brunel.ac.uk

[c] Research & Development, Bharat Heavy Electricals Limited, Tiruchirappalli, India.

Email: dr193683@gmail.com

Abstract

Thermal interface resistance of Thermoelectric Generator (TEG) plays a vital role in power production. Improving surface finish of contact surfaces, applying pressure between the contact surfaces and use of Thermal Interface Material (TIM) are few methods of reducing thermal resistance and thereby improving the efficiency of TEG. There is a need to evaluate the influence of these methods and use them optimally for TEG system. Experiments were carried out to study the influence of parameters such as thermal conductivity of TIM, contact pressure, surface roughness and heat source temperature on the voltage and power outputs from TEG. Experimental results are validated with simulations using mathematical heat transfer model and COMSOLTM Multiphysics numerical model. Appreciable agreement is seen between the experimental observations and model outputs. Experimental and model results indicate 0.6 W/mK as optimum thermal conductivity for TIM material. Hence, use of costly TIMs like MWCNT (Multi Wall Carbon Nano Tube) and copper nanoparticles may not be required for the selected application. The contact pressure and surface roughness have appreciable influence when air is used as TIM. These factors have insignificant influence for TIMs with higher thermal conductivity. Increase in heat source temperature increases voltage and power output of TEG.

Keywords: Thermal Interface Material, Thermoelectric Generator, Heat Transfer Model, COMSOL, Contact Pressure.

1. Introduction

Thermoelectricity, discovered in the 18th century, based on the principle of Seebeck effect, promoted the development of thermoelectric generator (TEG). Currently, the acceptability of the TEG is limited by its high capital cost and low energy conversion efficiency. Development of material science and emerging ideas since the 1990s, focused on improving the figure of merit (the ratio of the product of square of Seebeck coefficient, electrical conductivity and the operational temperature to the thermal conductivity) of TEG materials, which revived the hope for TEG to perform at par with the conventional heat engines. Recent advances have been reported in Nanoscale thermoelectric materials [1-3], doping methodology [4-6], organic thermoelectric materials [7], and oxide thermoelectric materials [8,9]. Commercially available TEG modules can achieve a maximum efficiency of 7% [10], which could reach 15% at a figure of merit of approximately 1.5 [11]. An availability of huge quantity of low temperature (< 200 °C) waste heat in several industries [12-14], will only be fortuitous if a TEG system is developed to exploit this low temperature waste heat. The potential of TEG system in conjunction with solar energy technologies is also reported [15, 16] in literature.

Thermal Interface Material (TIM) is critical to achieve a higher conversion efficiency in the TEG system. For obtaining maximum power, the thermal conductance of TIM interfaces with the heat source and sink has to be maximised, which will also allow the exploitation of lower temperature differences between two thermal contact surfaces. The TIM comprising of Carbon Nano Tube (CNT) [17-19] is a potential candidate. An ideal TIM would eliminate the air gap, resulting in zero temperature difference between the two contacting surfaces. This is not practically achievable, even though many studies have assumed so [20]. Astrain et al. [21] reported that a 10% decrease in thermal resistance can increase the power generated by up to 8%. Wang et al. [22] experimentally investigated and analysed the effects of the interface material and loading pressure factors on the thermal contact resistance and the performance of TEG.

Literature review indicates that no comprehensive study has been performed to evaluate and characterise the combined effects of contact pressure, surface roughness and thermal conductivity of TIM under varying heat source temperatures. Therefore, the objective of this paper is to optimize the thermal system for TEG applications by evaluating the effects of the aforementioned factors through a combined computer modelling and experimental programme. COMSOL™ Multiphysics has been employed for computer simulations and the model and simulation results have been validated against experimental results.

2. Experimentation

Experiments under varying conditions were conducted and the open circuit voltage and closed circuit power were measured. A schematic diagram of the experimental TEG set-up and its 3-D view are shown in Fig. 1(a) and Fig. 1(b) respectively. The experimental set-up used for the performance evaluation of TIM for TEG system is shown in Fig. 2. An electric heater was placed between a steel holding plate and an aluminium heat spreader plate to simulate the heat source. A K-type thermocouple of 1.5 mm diameter was placed in between the bottom of heat spreader plate and the electric heater to measure the heat source temperature (T_{hs}) which was maintained by a temperature controller through an electric resistance. Three TEGs were sandwiched between the aluminium heat spreader plate (heat source side) and an aluminium fin heat sink. K-type thermocouples were employed to measure heat spreader plate temperatures, T_{h1}, T_{h2} and T_{h3} and aluminium fin base plate temperature, T_{c1}, T_{c2} and T_{c3}. The contact area between the TEG and aluminium heat spreader plate on hot side and between TEG and aluminium fin plate on sink side were filled with Thermal Interface Material (TIM). During the experiments, the internal resistance of TEG module was matched with the external electric load (R_L) ensuring maximum power output. At this condition, the effect of influencing parameters such as interface contact pressure and surface roughness and thermal conductivity of TIM was evaluated. Table 1 provides the details of the TEG TIM test set up.

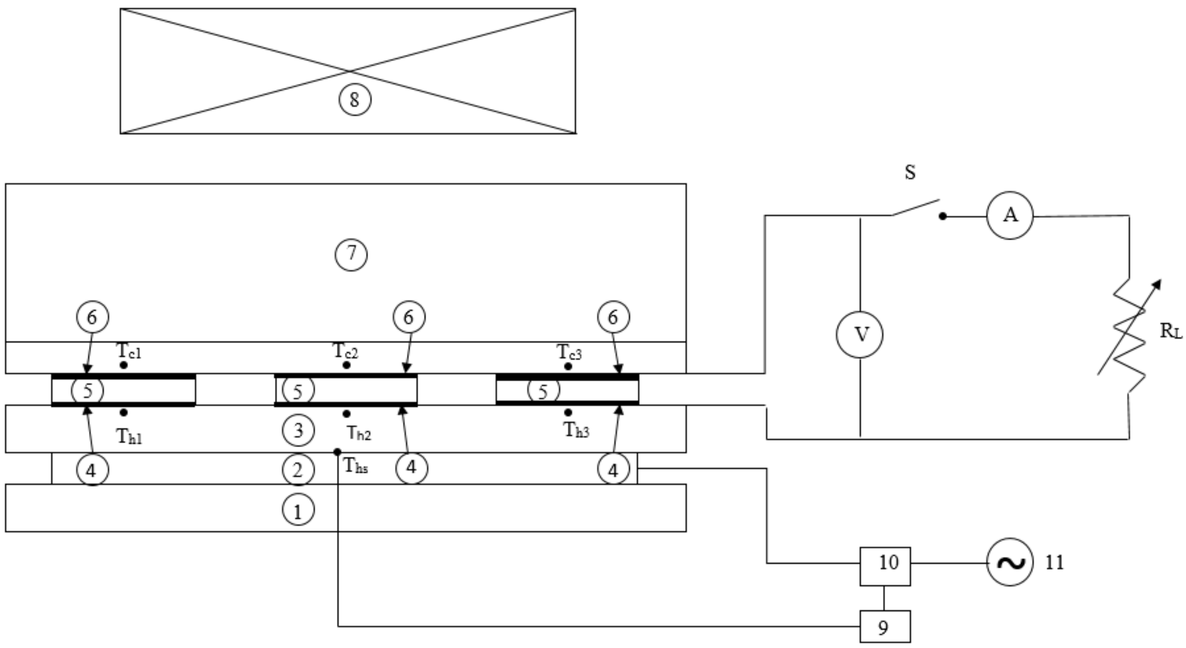

Fig. 1(a). A scheme of the experimental set up: 1 – Steel holding plate, 2. Electric heater, 3 – aluminium heat spreader plate, 4 – TEG hot side TIM, 5 – Thermoelectric generator module, 6 – TEG cold side TIM , 7 – aluminium fin heat sink, 8 – Cooling fan, 9 – Temperature controller, 10 – Electric contactor, 11 – Electric power source, V – Voltmeter, A – Ammeter, S- Electric switch, R_L – Variable external load resistor, T_{hs} –

Heat source temperature (°C), T_{h1}, T_{h2} and T_{h3} – heat spreader temperature sensors, T_{c1}, T_{c2} and T_{c3} - fin base plate temperature sensors

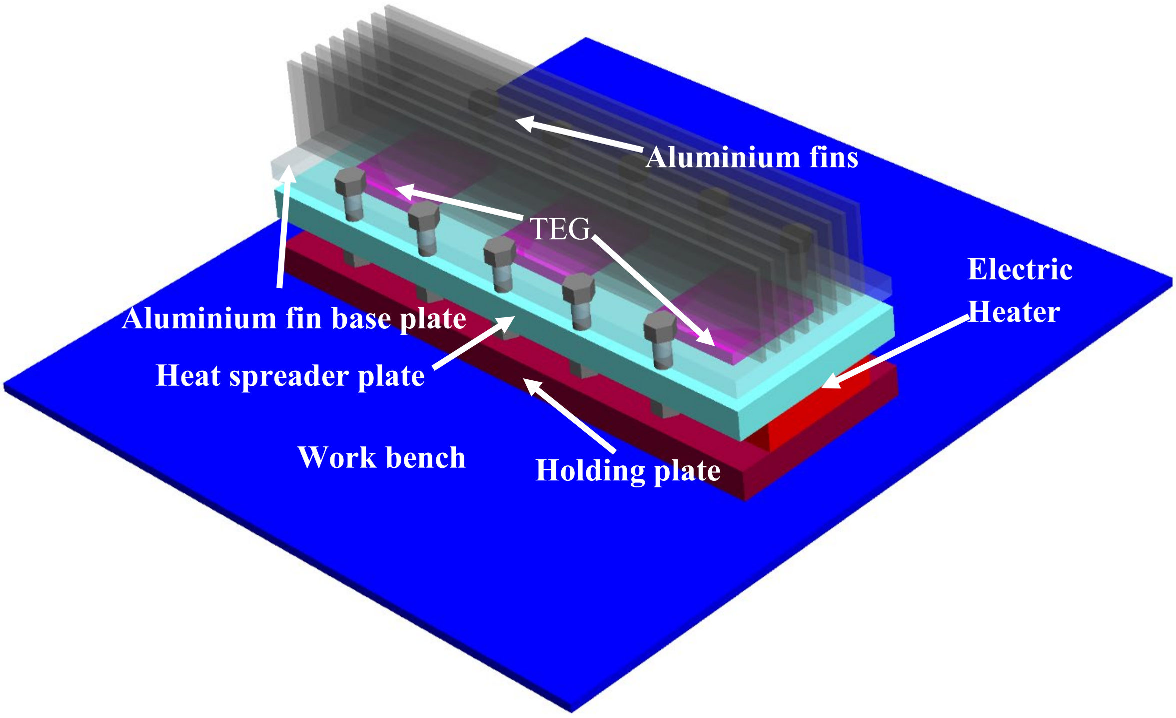

Fig. 1(b) 3D view of the schematic for TEG experimental set-up

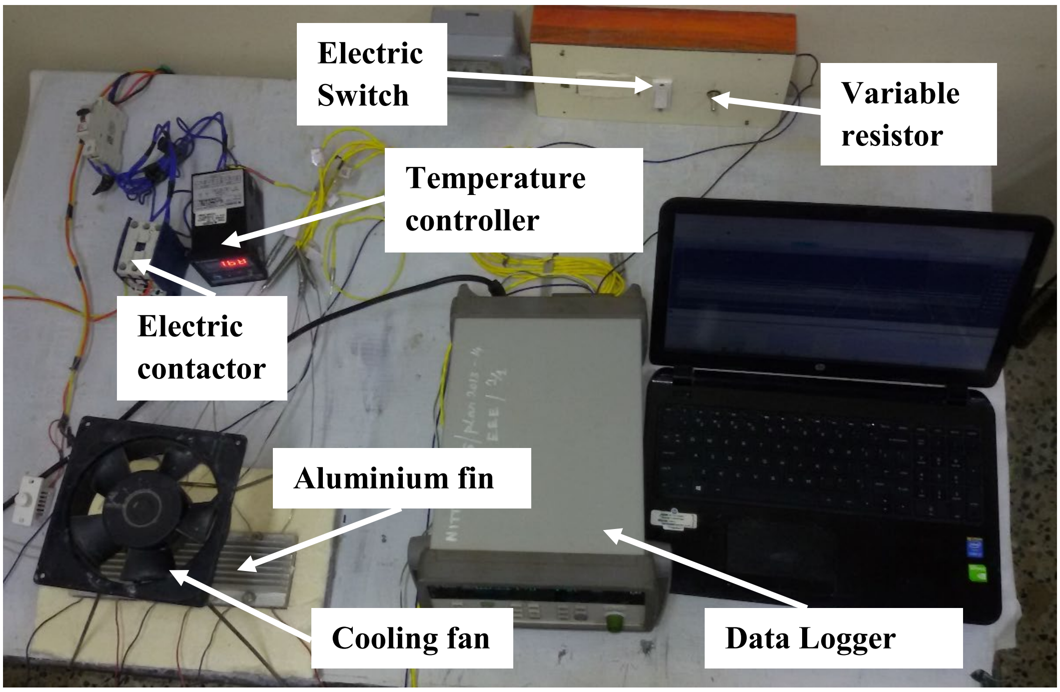

Fig. 2 Experimental set up

Table 1 Details of the TEG TIM test setup

Sl No	Description	Value
	Heat source	
1	Electric heater	240×40x10 mm
2	Steel holding plate	240x40x10 mm
3	Aluminum heat spreader plate	240x77x10 mm
	TEG	
4	P and N junction leg	1.5x1.5x1.5 mm
5	Top and bottom copper connecting bar	3.5x1.5x0.5 mm
6	Top and bottom ceramic plate	40x40x0.75 mm
	Heat sink	
7	Fin base plate	240x77x4 mm
8	Fin thickness	2 mm
9	Fin length	240 mm
10	Fin gap	5 mm
11	Number of fins	8 Nos
	Electric load	
12	External electric load resistor	36x10x0.5 mm

2.1 Experimental variables

2.1.1 Interfacial contact pressure

The experimental set-up employed for measuring contact pressure on TIM is shown in Fig. 3 with Table 1 presenting the geometric details. The aluminium fin base plate was joined with heat spreading plate using M4 bolts.

Considering the challenges in measuring the interfacial contact pressure, a calibration dataset between bolt torque and contact pressure was created using a pressure measuring film (Fuji film prescale, Type: LLW) between the aluminium plate/fin and TEG. The contact pressure measured for different applied torques is shown in Fig. 4.

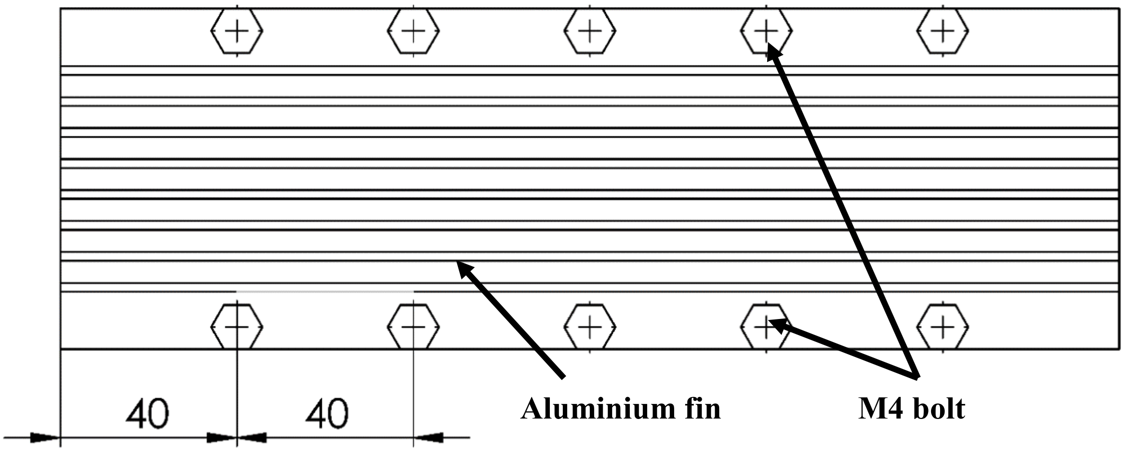

Fig. 3 Top view of the experimental set-up arranged for measuring contact pressure (dimensions in mm)

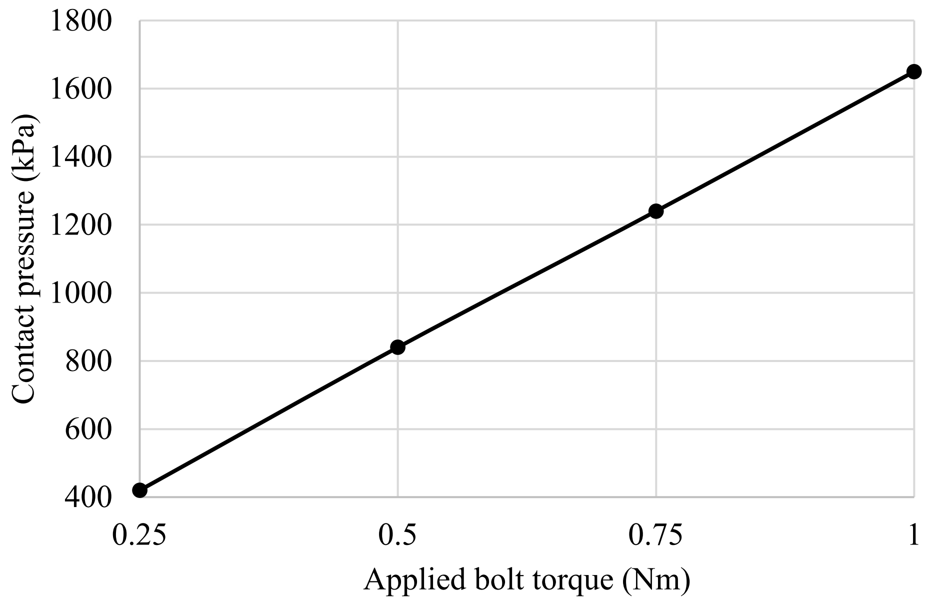

Fig. 4 Measured contact pressure as a function of applied torque

2.1.2 Thermal conductivity of different TIM's

The silicon grease and silicone oil were used for this study as a base material with nanoparticles (NPs) such as Multiwall Carbon Nanotube (MWCNT) and copper added in varying proportions to improve the thermal conductivity of the TIM. Silicone grease, a mixture of Silicone grease with 0.5 weight percentage (%wt) of MWCNT and a mixture of Silicone oil with 40 %wt of Cu NPs are respectively shown in Fig. 5(a), 5(b) and 5(c). Their thermal conductivity was measured using Laser Flash Apparatus (LFA 457 microflash®, Netzsch, Germany) and are presented in Table 2.

(a) **(b)** **(c)**

Fig. 5 Thermal Interface Materials (TIMs) employed in this study

Table 2 Thermal conductivity of TIM's

Sl No	Thermal Interface Material	Thermal conductivity (k_{tim}) (W/m.K)
1	Silicone grease	0.6
2	Silicone grease + 0.5 %wt MWCNT	0.9
3	Silicone Oil + 40 %wt Cu NP	4.2

2.1.3 Surface Roughness of base and TEG surface material

The aluminium heat spreader plate and aluminium fin base plate used in the experiments had three variations in surface roughness viz., 0.8 μ, 3.12 μ and 6 μ as measured by White Light Interferometer (Rtec instruments, USA). The surface roughness of TEG was constant at 1.3 μ.

3 Modelling

3.1 Governing equation for Numerical model (NM)

3.1.1. Heat exchanger model

Energy equation (Laplace equation) for thermoelectric modules for various temperature fields is described in Eq. (1).

$$\nabla . \nabla T_{hs} = 0 \quad (1)$$

where T_{hs} is the heat source surface temperature

Temperature of the exposed heat source surface (T_{hs}) was used as the boundary condition. Rate of heat transferred from cold side of TEGs (Q_c in W) by convection was calculated using Eq. (2).

$$Q_c = h_{camb} A_{eff} (T_{hs} - T_a) \quad (2)$$

where h_{camb} is the heat transfer coefficient between fin and ambient, A_{eff} is the fin effective area, T_a is the ambient temperature.

3.1.2 Thermal contact model

Eqs. (3) and (4) provide the conductance (h) at the interface of two bodies in contact [23].

$$-n_d . (-k_d \nabla T_d) = -h(T_u - T_d) \quad (3)$$

$$-n_u . (-k_u \nabla T_u) = -h(T_d - T_u) \quad (4)$$

where u and d subscripts denote the upside and downside of the slit respectively, k denotes the thermal conductivity, T is the temperature, n is the normal vector to the boundary and the conductance (h) at the interface of two bodies in contact can be written Eq. (5)

$$h = h_c + h_g \tag{5}$$

where h_c is the contact conductance and h_g the gap conductance.

The contact conductance (h_c) described by Eq. (6) is the heat flux across the surfaces in contact [24].

$$h_c = \frac{1}{R_c A_a} = 1.25 k_s \left(\frac{m_s}{\sigma}\right)\left(\frac{P_{tim}}{H_c}\right)^{0.95} \tag{6}$$

where R_c is the thermal interface resistance due to contact, A_a is the apparent contact area of joining surfaces, P_{tim} the contact pressure and H_c the micro-hardness of softer contact surface of the two surfaces in contact.

The effective Root Mean Square (RMS) of surface roughness (σ) is given as:

$$\sigma = \sqrt{{\sigma_{Al}}^2 + {\sigma_{teg}}^2} \tag{7}$$

σ_{Al} is the surface roughness plate in contact with TEG, σ_{teg} is the surface roughness of TEG

m_s is the absolute mean asperity slope obtained from slopes m_{Al} and m_{teg} for two contacting surfaces. The effective absolute mean asperity slope (m_i) is obtained using Eq. (8).

$$m_i = 0.152(\sigma_i)^{0.44} \tag{8}$$

where σ_i is the effective absolute surface roughness

$$m_s = \sqrt{{m_{Al}}^2 + {m_{teg}}^2}$$

Then, the thermal conductivity of the material, k_s [23], could be calculated using Eq. (9).

$$\frac{2}{k_s} = \frac{1}{(k_u\, n_u)\,.\; n_u} + \frac{1}{(k_d\, n_d)\,.\; n_d} \tag{9}$$

where u and d subscripts denote the upside and downside of the slit refer respectively, k denotes the thermal conductivity and n is the normal vector to the boundary.

For parallel plate, gap conductance (h_g) could be calculated by using Eqs. (10) - (13) [23 and 24].

$$h_g = \frac{1}{R_g A_a} = \frac{k_{tim}}{Y+M} \tag{10}$$

where Y is the layer thickness of the TIM, R_g is the thermal interface resistance due to gap and k_{tim} is the thermal conductivity of TIM.

According to simple power law relation [17], the mean plane separation Y will be

$$Y = 1.53\sigma \left(\frac{P_{tim}}{H_c}\right)^{-0.097} \quad (11)$$

$$M = 0, \text{ for TIM filled gap,} \quad (12)$$

where M is a constant and $M = \alpha_a \beta \wedge$, for the gap filled by air ($k_{tim} = k_{air}$). (13)

For air, gas parameters $\alpha_a = 2.4$, $\beta = 1.7$ and molecular free path ($\wedge$) = 0.06 µm.

The thermal interface conductance h for both hot and cold sides of TEG could be found by using Eqs. (5) - (13).

3.1.3 Coupled field model

Accounting for the coupling mechanisms of Seebeck, Peltier and Thomson effects between electrical and thermal fields, a fully coupled-field model was developed by generating governing equations under steady-state conditions for both electrical potential profiles and temperature in the absence of input magnetic field [25].

By taking Joule heating into account in the process, the equation for energy conservation is given by

$$\nabla (k \,.\, \nabla T) - T \,.\, J \,.\, \frac{\partial \alpha}{\partial T} + \rho \,.\, J = 0 \quad (14)$$

where ρ is the electrical resistivity, k is the thermal conductivity of TEG leg, T is the temperature, J is the current density and α is the Seebeck coefficient.

Now, applying thermoelectric effect into the coupling of heat flow equation and electric charge continuity equation [25],

$$\nabla \,.\, J = 0 \quad (15)$$

$$q = [\Pi] \,.\, J - [k] \,.\, \nabla T \quad (16)$$

$$J = [\sigma_e] \,.\, (E - [\alpha] \,.\, \nabla T) \quad (17)$$

where $[\sigma_e]$ is the electrical conductivity of TEG leg matrix, [k] is the thermal conductivity of TEG leg matrix, [α] is the Seebeck coefficient of TEG leg matrix and [Π] is the Peltier coefficient of TEG leg matrix which depends on T[α]

In the absence of time varying magnetic field, E becomes irrotational and was derived from an electric scalar potential (ϕ)

$$E = -\nabla \phi \quad (18)$$

Hence, electric power (P_o) expression is given by

$$P_o = \frac{V_{oc}^2}{2(R_{teg} + R_L)} \quad (19)$$

where V_{oc} is the open circuit voltage, R_{teg} is the internal resistance of TEG, R_L is the external load resistance.

For obtaining maximum electric power, $R_L = R_{teg}$

The thermoelectric equations provided above were used for determining the five state vector parameters Q_h, Q_c, T_h, T_c and I_o for TEGs.

3.2 Computer model and the boundary conditions employed

A 3D TEG system (see Table 1 for geometric details), was modelled using COMSOL™ Multiphysics for cold and hot side thermal contact resistance. Fig. 6 shows the 3D mesh for the overall TEG system employed. A 3D mesh (Fig. 6(a)) and a fine mesh (Fig. 6(b)) were used in the TEG P and N junction elements to capture a realistic thermoelectric effect.

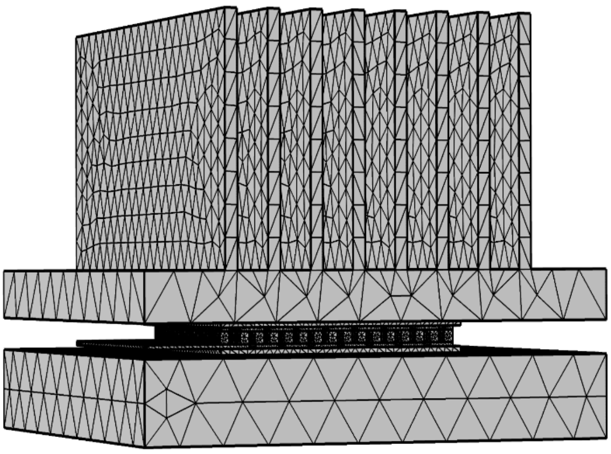

Fig. 6(a) 3D mesh for TEG system of TIM

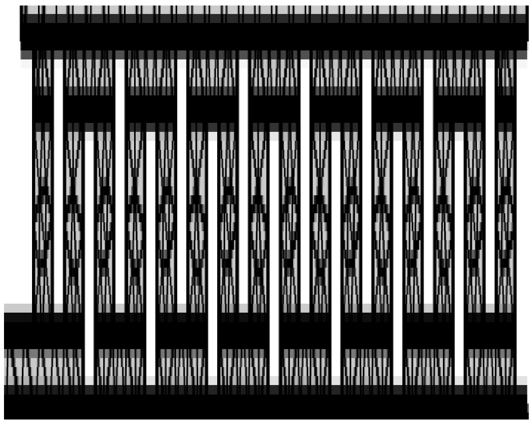

Fig. 6(b) Zoomed mesh TEG P and N junction elements

Principles of heat transfer in solids, thermoelectric effect and Yovanovich correlation [24] were employed in the analysis. Table 3 provides the material properties and Table 4 the boundary conditions employed.

Table 3 Material properties of the TEG-TIM components employed

Sl No	Description	Value
	Base plate and heat sink	
1	Thermal conductivity of aluminum base plate	201 W/mK
2	Thermal conductivity of aluminum heat sink	201 W/mK
	TEG	

3	Thermal conductivity of top and bottom alumina plate	40 W/mK
4	Thermal conductivity of top and bottom copper bar	401 W/mK
5	Seebeck coefficient of P-junction	0.0002 V/K
6	Seebeck coefficient of N-junction	0.0002 V/K
7	Thermal conductivity of P-junction	1.7 W/mK
8	Thermal conductivity of N-junction	1.7 W/mK
9	Resistivity of P-junction	$1X10^{-5}$ Ωm
10	Resistivity of N-junction	$1X10^{-5}$ Ωm
11	Resistivity of top and bottom copper bar	$2.27X10^{-8}$ Ωm

Table 4 Boundary conditions employed

Sl No	Description	Value
1	Base plate hot source temperature (T_{hs})	100, 150, 200 ˚C
2	Surface roughness of TEG (σ_{teg})	1.3 µ
3	Surface roughness of aluminium base and fin (σ_{Al})	0.8, 3.1,6 µ
4	Contact pressure (P_{tim})	420, 840, 1240,1650 kPa
5	Surface hardness of aluminium material (H_{Al})	1060 MPa
6	Ambient temperature (T_a)	35˚C
7	Combined heat transfer co-efficient (fin surface to ambient) (h_{camb})	25 W/m^2K
8	Low potential on N-junction bottom copper bar	0 V
9	Electric conductivity of electric load resistor at 200 ˚C, 150 ˚C, 100 ˚C for TEG internal resistance equal to load resistance	2955, 2585, 2501 S/m

3.3 Performance coefficients of TEG

Seebeck effect states that for an electrical conductor, the temperature difference across the conductor will cause the induction of an electric current and TEG works using this principle. In addition, Peltier effect, Fourier effect and Joule effect also play a significant role in a TEG module.

TEG performance can be described by considering the Seebeck coefficient, its internal electrical resistance and thermal conductance. The hot side thermal power input (Q_h in W) and the cold side thermal power output (Q_c in W) were calculated by using Eqs. (20) - (29) [26].

$$Q_h = \alpha I_o T_h + K(T_h - T_c) - \frac{I_o^2 R_{teg}}{2} \tag{20}$$

$$Q_c = \alpha I_o T_c + K(T_h - T_c) + \frac{I_o^2 R_{teg}}{2} \tag{21}$$

where T_h is the TEG hot side temperature, T_c is the TEG cold side temperature, I_o is the output current and

α is the Seebeck coefficient (V/K) of the TEG module can be described as:

$$\alpha = N_c \alpha(T) \quad (22)$$

where N_c is module series connected couple count and α(T) is the Seebeck coefficient of the P-N couple

The internal resistance (R_{teg}) of the TEG module is given by

$$R_{teg} = \frac{N_c L \rho(T)}{A_{ct}} \quad (23)$$

where L is the height of P-type and N-type elements and A_{ct} the cross-sectional area of P-type / N-type elements and ρ(T) is the electrical resistivity of the P-N couple

The thermal conductance (K) of the TEG module is given as

$$K = \frac{N_c A_{ct} k(T)}{H_l} \quad (24)$$

where k(T) is the thermal conductivity of the P-N couple and H_l is the height of the TEG element

The power generated by the TEG system was calculated from heat flux variation or from the product of voltage and output current.

$$P_o = V_o I_o = Q_h - Q_c \quad (25)$$

where P_o is the electric power output and V_o is the output voltage

Using Eq. (20) and Eq. (21), Eq. (25) can be written as

$$P_o = Q_h - Q_c = \alpha I_o (T_h - T_c) - {I_o}^2 R_{teg} \quad (26)$$

The output voltage can be found from Eq. (26)

$$V_o = \frac{P_o}{I_o} = \alpha(T_h - T_c) - I_o R_{teg} \quad (27)$$

During open circuit condition (I_o=0), open circuit voltage (V_{oc}) can be deduced from Eq. (27) as shown in Eq. (28).

$$V_{oc} = \alpha(T_h - T_c) \quad (28)$$

Hence, the output current (I_o) was calculated by 1st order partial derivative of Eq. (26) and equating it to zero.

$$I_o = \frac{V_{oc}}{R_g + R_L} = \frac{\alpha(T_h - T_c)}{R_g + R_L} \quad (29)$$

where R_L is the variable electrical load resistance connected externally to the circuit.

3.4 Heat Transfer model of TEG with TIM's.

In this study, the A plate fin heat sink with a fan on the cold side was used to minimize the TEG cold side temperature.

The developed heat transfer model accounted for the thermal interface resistances of hot and cold sides of TEG. Thermal resistance on hot side comprised of interface thermal resistance (R_{hi}) and heat spreading plate thermal resistance (R_{sp}). Thermal resistance on cold sides comprised of interface thermal resistance (R_{ci}), fin base plate thermal resistance (R_{bf}) and fin to air convective thermal resistance (R_{camb}).

The thermal resistances of the system from hot side to cold side of the TEG are as shown in Fig. 7.

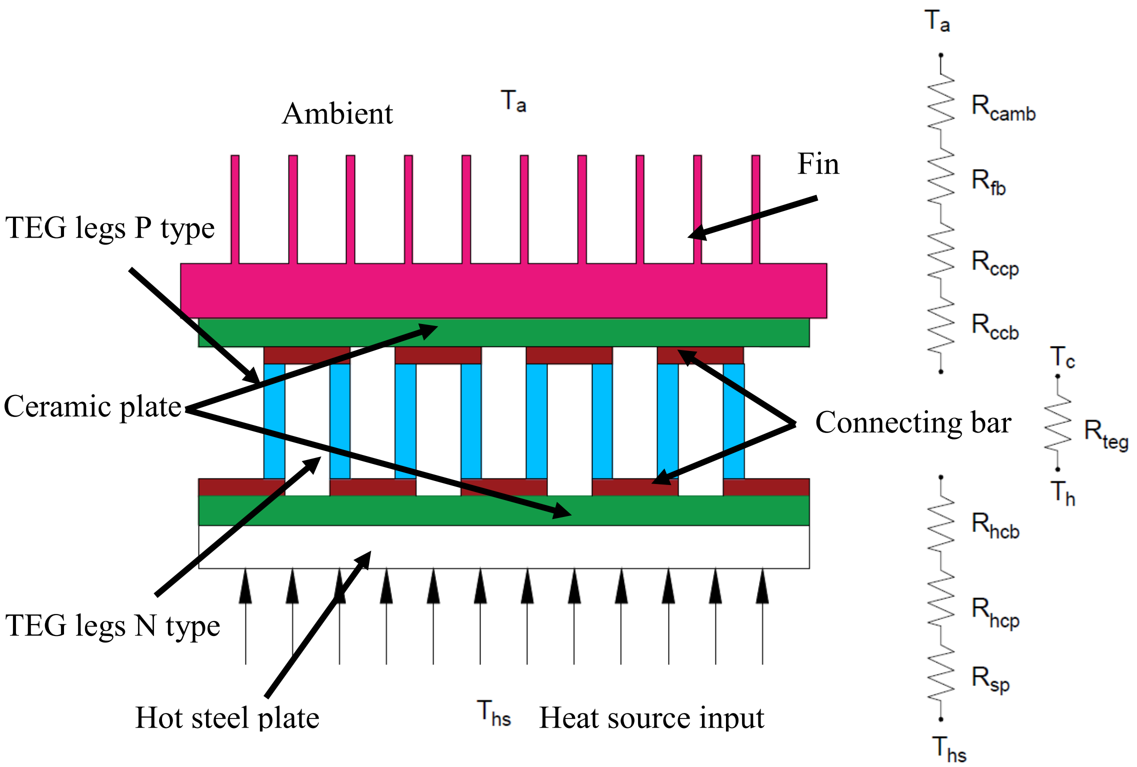

Fig. 7 Details on thermal resistances of TEG system

Thermal resistance of hot base plate was calculated from Eq. (30).

$$R_{sp} = \frac{t_{sp}}{k_{sp}A_{sp}} = \frac{t_{sp}}{k_{sp}W_{sp}L_{sp}} \quad (30)$$

where R_{sp} is the thermal resistance of heat spreader plate, k_{sp}, t_{sp}, A_{sp}, W_{sp} and L_{sp} are the thermal conductivity, thickness, surface area, width and length of the heat spreader plate respectively.

Introduction of the TIM reduces air gap and increases thermal conductivity and hence reduces the temperature difference contact surfaces. The following factors influence the interface resistances on hot and cold sides of TEG,:

1. Thermal conductivity of TIM (k_{tim})
2. Surface roughness (σ)
3. Contact pressure (P_{tim})

The contact and gap resistances (R_c and R_g) of hot and cold side of TEG could be obtained using Eqs. (5) - (13). The combined resistances of hot (R_{hi}) or cold (R_{ci}) side could be obtained using Eq. (31).

$$\frac{1}{R_i} = \frac{1}{R_c} + \frac{1}{R_g} \tag{31}$$

The total interface resistance (R_i) is expressed as in Eq. (31) considering the following assumptions:

1. The surfaces are microscopically rough and macroscopically conforming.
2. The plastic deformation occurs in the softer solid and the flow pressure is constant.
3. The contact spots are isothermal.
4. The total heat flow rate through each flux tube can be separated into two independent heat flow rates: contact spot and gap flow rates.
5. The effective gap thickness is dependent upon the surface roughness and the relative contact pressure.
6. Non-continuum gas effects must be taken into account.
7. The surfaces are clean and free from oxides, films, etc.
8. Radiative heat transfer is negligible.

The fin base plate resistance (R_{fb}) could be expressed as

$$R_{fb} = \frac{t_{fb}}{k_{fb}A_{fb}} = \frac{t_{fb}}{k_{fb}W_{fb}L_{fb}} \tag{32}$$

where R_{fb} is the fin base plate thermal resistance, k_{fb}, t_{fb}, A_{fb}, W_{fb} and L_{fb} are the thermal conductivity, thickness, surface area, width and length of the fin base plate respectively.

Ambient thermal resistance (R_{camb}) could be expressed as

$$R_{camb} = \frac{1}{h_{camb}A_{eff}} \tag{33}$$

where h_{camb} is the combined heat transfer co-efficient which could be expressed as,

$$h_{camb} = 5.678\left\{a + b\left[\frac{(294.26V_w/(T_a))}{0.3048}\right]^n\right\} \quad (34)$$

where a = 0.99, b = 0.21, n=1 for $V_w < 4.88$ m/s

a = 0, b = 0.5, n=0.7 for $4.88 \leq V_w \geq 30.48$ m/s

and V_w is the wind velocity, T_a is the ambient temperature

For plate fin heat sink effective heat transfer area (A_{eff}) and fin efficiency (η_f) could be obtained by using Eqs. (35) - (37).

Plate fin heat sink effective heat transfer area,

$$A_{eff} = (\eta_f(2N_fL_fH_f) + (N_f - 1)bL_f) \quad (35)$$

where N_f is the number of fin, L_f is the length of the fin, H_f is the height of the fin, b is the tunnel width.

Fin efficiency, $\eta_f = \frac{\tanh(mH_f)}{mH_f}$ (36)

$$m = \sqrt{\frac{h_{camb}Xp}{k_fXt_f}} \quad (37)$$

where p is the perimeter of the fin tip, k_f is the thermal conductivity of fin and t_f is the thickness of the fin.

U_h, A_h and U_c, A_c are overall heat transfer coefficient and effective heat transfer area on hot and cold side respectively could be obtained by using Eqs. (38) and (39).

$$U_hA_h = \frac{1}{R_{sp}+R_{hi}} \quad (38)$$

$$U_cA_c = \frac{1}{R_{ci}+R_{fb}+R_{camb}} \quad (39)$$

The heat supplied (Q_h) to hot side and heat dissipated (Q_c) out through cold side were given by the equations:

$$Q_h = U_hA_h(T_{hs} - T_h) \quad (40)$$

$$Q_c = U_cA_c(T_c - T_a) \quad (41)$$

By equating Eq. (20) with Eq. (40) and Eq. (21) with Eq. (42), the expressions for T_h and T_c were arrived as follows:

$$T_h = \frac{U_hA_hT_{hs}+KT_c+\frac{I_0^2R_{teg}}{2}}{\alpha I_o+K+U_hA_h} \quad (42)$$

$$T_c = \frac{U_c A_c T_a + K T_h + \frac{I_o^2 R_{teg}}{2}}{U_c A_c + K - \alpha I_o} \quad (43)$$

where U_c is the overall heat transfer coefficient on cold side and U_h is the overall heat transfer coefficient on hot side.

T_h and T_c were iteratively computed for different source temperatures and other variables. The expression for I_o was obtained by substituting T_{hs}, T_a, α and R_{teg} into Eq. (29). Consequently, Q_h, Q_c, P_o and V_o expressions were obtained by substituting T_h, T_c, α, R_{teg}, K and I_o into Eqs. (20), (21), (42) and (43).

4 Results and discussion

4.1 Modelling analysis

The commercially available COMSOL™ multiphysics numerical model having in-built governing equations discussed in 3.1 was simulated for all material properties and boundary conditions of TEG-TIM test set up as given in Table 3 and Table 4 respectively. Outputs at both open and closed circuit conditions were obtained for each variation.

Fig. 8(a) and 9(a) show the temperature and open circuit voltage contours respectively for a case with no TIM (only air gap) and T_{hs} = 200 °C, σ = 1.53 μ and P_{tim} = 1650 kPa.

Fig. 8(b) and 9(b) show the temperature and open circuit voltage contours respectively for a case with Silica oil + 40 %wt Cu nanoparticle as TIM and T_{hs} = 200 °C, σ = 1.53 μ and P_{tim} = 1650 kPa.

Maroon colour shows the highest temperature/voltage while blue colour indicates lowest temperature/voltage in the above pictures. Comparison of the colour contours with and without TIM in the interface zone between the top of TEG and the bottom of fin plate and that between the bottom surface of TEG and top of hot plate reveal appreciable reduction in temperatures at the interfaces due to the introduction of TIM leading to an increased open circuit voltage in the output. Similar improvement is seen in the contours for closed circuit.

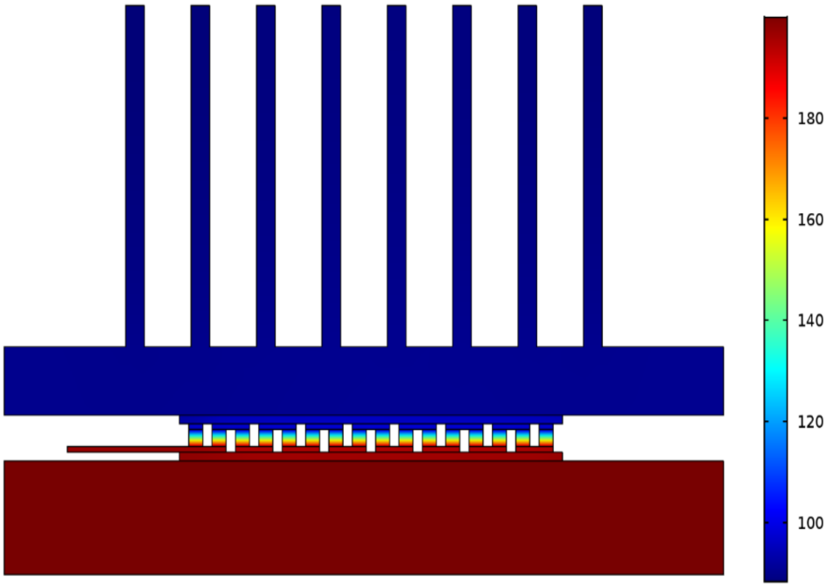

Fig. 8(a) Temperature contour at open circuit condition for no TIM (only entrapped air) and T_{hs} = 200 °C, σ = 1.53 μ and P_{tim} = 1650 kPa

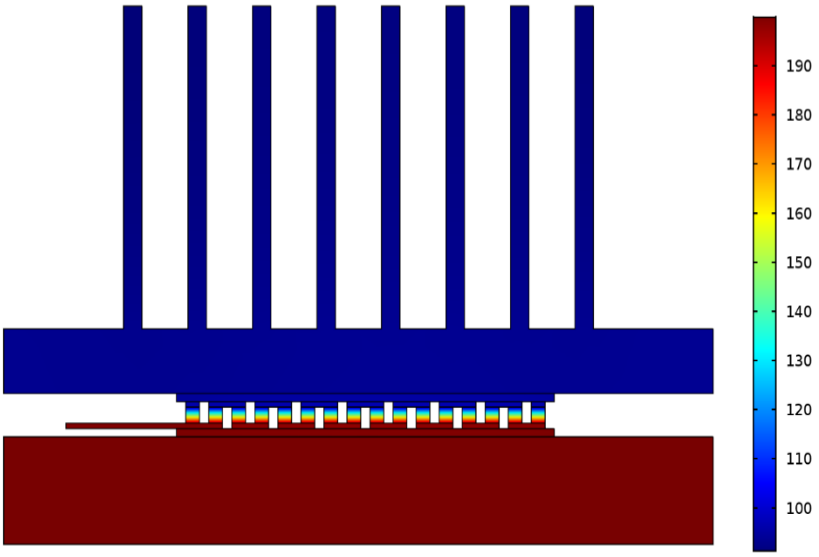

Fig. 8(b) Temperature contour at open circuit condition for Silica Oil+ 40% Cu Nanoparticle (k_{tim} = 4.2 W/mK) as TIM and T_{hs} = 200 °C, σ = 1.53 μ and P_{tim} = 1650 kPa

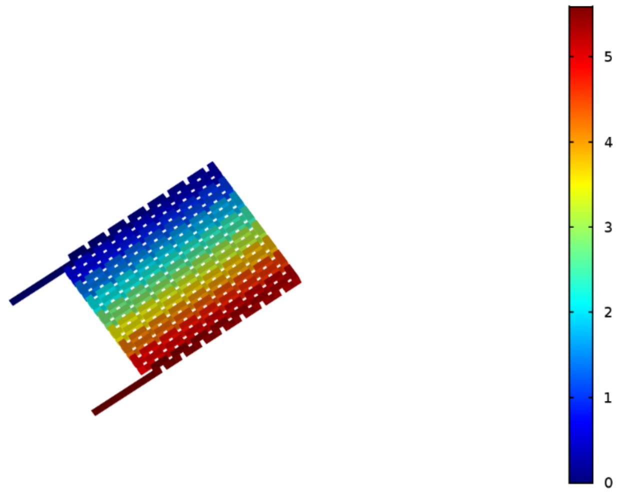

Fig. 9(a) Voltage contour at open circuit condition for no TIM (only entrapped air) and T_{hs} = 200 °C, σ = 1.53 μ and P_{tim} = 1650 kPa

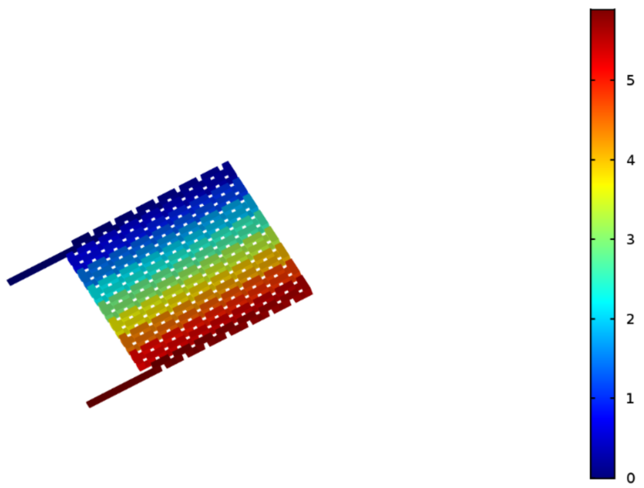

Fig. 9(b) Voltage contour at open circuit condition for Silica Oil+ 40% Cu Nanoparticle (k_{tim} = 4.2 W/mK) as TIM and T_{hs} = 200 °C, σ = 1.53 μ and P_{tim} = 1650 kPa

Fig. 10(a) and 11(a) show the temperature and closed circuit voltage contours respectively for a case with no TIM (only air gap) and T_{hs} = 200 °C, σ = 1.53 μ and P_{tim} = 1650 kPa.

Fig. 10(b) and 11(b) show the temperature and closed circuit voltage contours respectively for a case with Silica oil + 40 %wt Cu nanoparticle as TIM and T_{hs} = 200 °C, σ = 1.53 μ and P_{tim} = 1650 kPa.

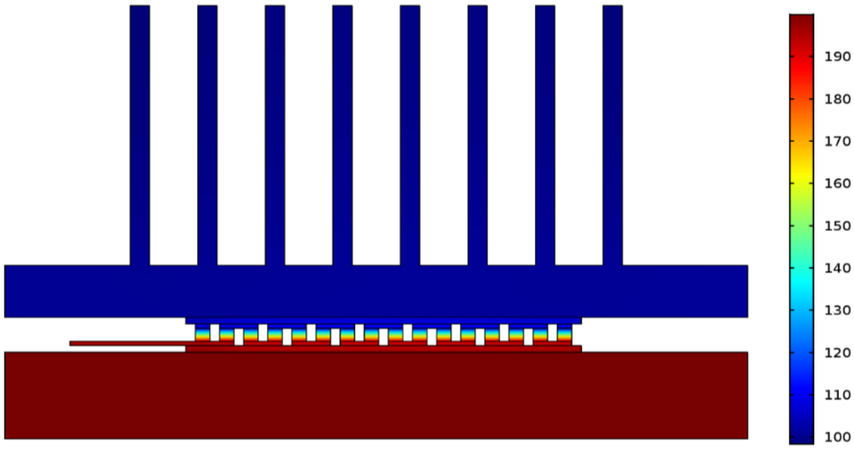

Fig. 10(a) Temperature contour at closed circuit condition for no TIM (only entrapped air) and T_{hs} = 200 °C, σ = 1.53 μ and P_{tim} = 1650 kPa

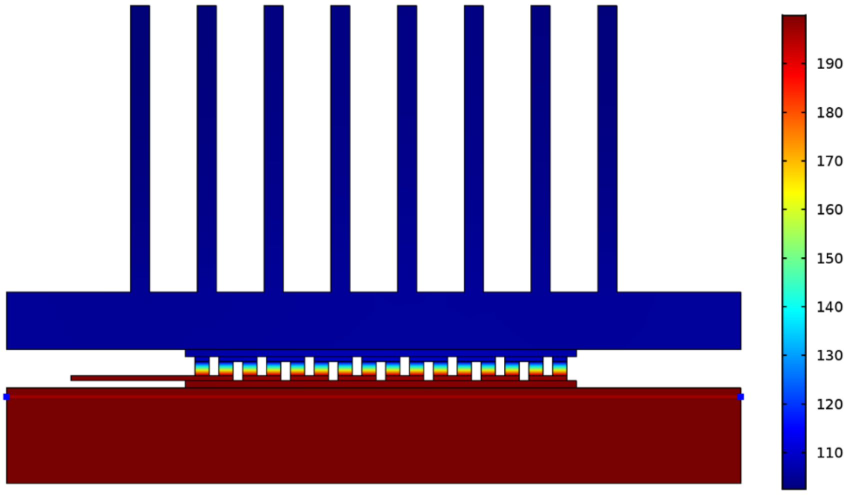

Fig. 10(b) Temperature contour at closed circuit condition for Silica Oil+ 40% Cu Nanoparticle (k_{tim} = 4.2 W/mK) as TIM and T_{hs} = 200 °C, σ = 1.53 μ and P_{tim} = 1650 kPa

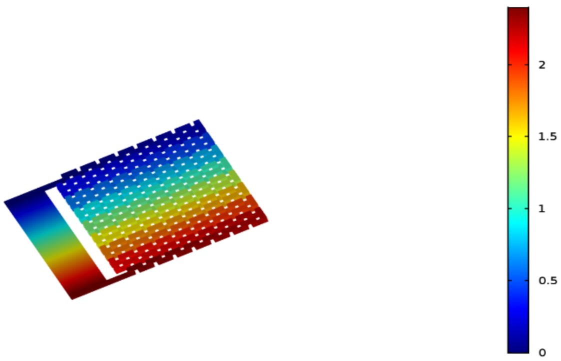

Fig. 11(a) Voltage contour of closed circuit condition for no TIM (only entrapped air) and T_{hs} = 200 °C, σ = 1.53 μ and P_{tim} = 1650 kPa

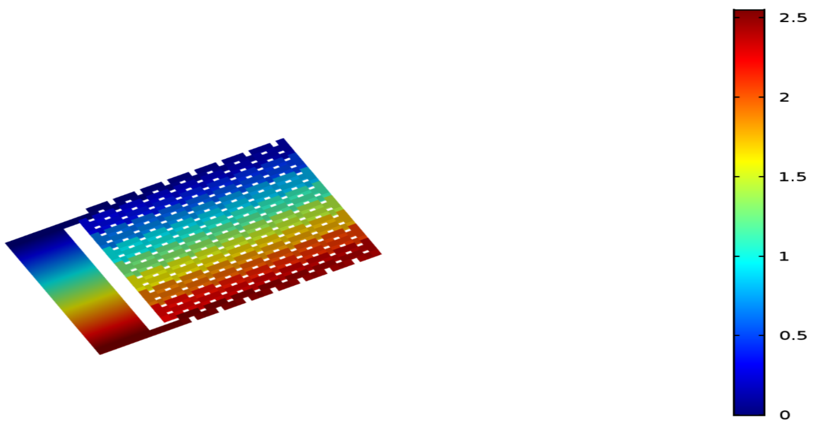

Fig. 11(b) Voltage contour of closed circuit condition for Silica Oil+ 40% Cu Nanoparticle (k_{tim} = 4.2 W/mK) as TIM and T_{hs} = 200 °C, σ = 1.53 μ and P_{tim} = 1650 kPa

4.2 Comparison of the model outputs with experimental data and evaluation of the impact of various parameters on the performance of TEG

Experiments and model outputs for varying thermal conductivities of 0.025, 0.6, 0.9 and 4.2 W/mK for TIM at hot side temperatures of 100, 150 and 200 °C, contact pressures of 420, 840, 1240 and 1650 kPa and surface roughness of 0.8, 3.1 and 6μ were compared for open circuit voltage and power output of TEG.

4.2.1 Influence of thermal conductivity

Fig. 12 and Fig. 13 show typical trends of open circuit voltage and closed circuit power outputs of TEG with respect to thermal conductivity of TIM keeping the other variables constant as shown in the respective figures. Analysis of the trends indicates steep increase in voltage and power outputs upto a thermal conductivity of 0.6 W/mK compared with that of air having a thermal conductivity of 0.025 W/mK and subsequent increase in outputs are very little for the increases in thermal conductivities to 0.9 and 4.2 W/mK. Though the trends of outputs of both models are in line with experimental data, the outputs of COMSOL^{TM} model is in close agreement with experiments with marginal deviation in the range 0.3 to 2.6 % for open circuit voltage and 0.5 to 3.1 % for electric power output. The outputs of heat transfer model comparatively deviate in the range of 2.3 to 5.9 % for open circuit voltage and 3.3 to 11.3 % for electric power output when compared to the experimental data.

It is clear from the data that the TIM fills up the unnoticeable surface undulations, establishes better connectivity and conductivity between the mating surfaces and thus improves the performance of TEG by 10 to 20%. The data has also revealed that the use of TIM with a thermal conductivity higher than 0.6 W/mK has only marginal improvement in the performance.

4.2.2 Influence of contact pressure

Fig. 14 and Fig. 15 show typical trends of open circuit voltage and closed circuit power outputs of TEG with respect to contact pressure between the spreading plates and TIM keeping the other variables constant as shown in the respective figures. The analysis of the trends indicates progressive improvements in voltage and power outputs at all conditions for a case with no TIM (only entrapped air) and the pressure requirement is higher for a rough surface than a smooth surface. Contact pressure does not have any effect at any condition for TIMs having higher thermal conductivities in the range of 0.6 to 4.2 W/mK.

4.2.3 Influence of surface roughness

Fig. 16 and Fig. 17 show typical trends of open circuit voltage and closed circuit power outputs of TEG with respect to surface roughness of heat spreading aluminium plates keeping the other variables constant as shown in the respective figures. The analysis indicated that the surface roughness is influential only when air is used as TIM and not for other TIMs having higher thermal conductivities.

4.2.4 Influence of heat source temperature

Fig. 18 and Fig. 19 show typical trends of open circuit voltage and closed circuit power outputs of TEG with respect to hot side temperatures keeping the other variables constant as shown in the respective figures. The results indicate that irrespective of the TIM, the open circuit voltage and electric power output keep increasing with increase in source temperature. However, the outputs are higher with the use of TIMs with higher thermal conductivity than air.

Recently, Wang et al. [22] analysed the performance of TEG with air and thermal grease as TIM under varying contact pressures of up to 765 kPa, however, the effect of roughness of the contact surfaces was ignored. This aspect has been covered by the present study and approximately 12% increase in power output with the use of TIM (2.01 W with air to 2.25 W with TIM at a contact pressure of 420 kPa) is being reported. Wang et al. [22] reported an increase in power output with an increase in contact pressure even when TIM was used. Whereas, what this paper reports here is an increase in power output with an increase in contact pressure only with air and it remains almost constant at all contact pressures when TIM is used.

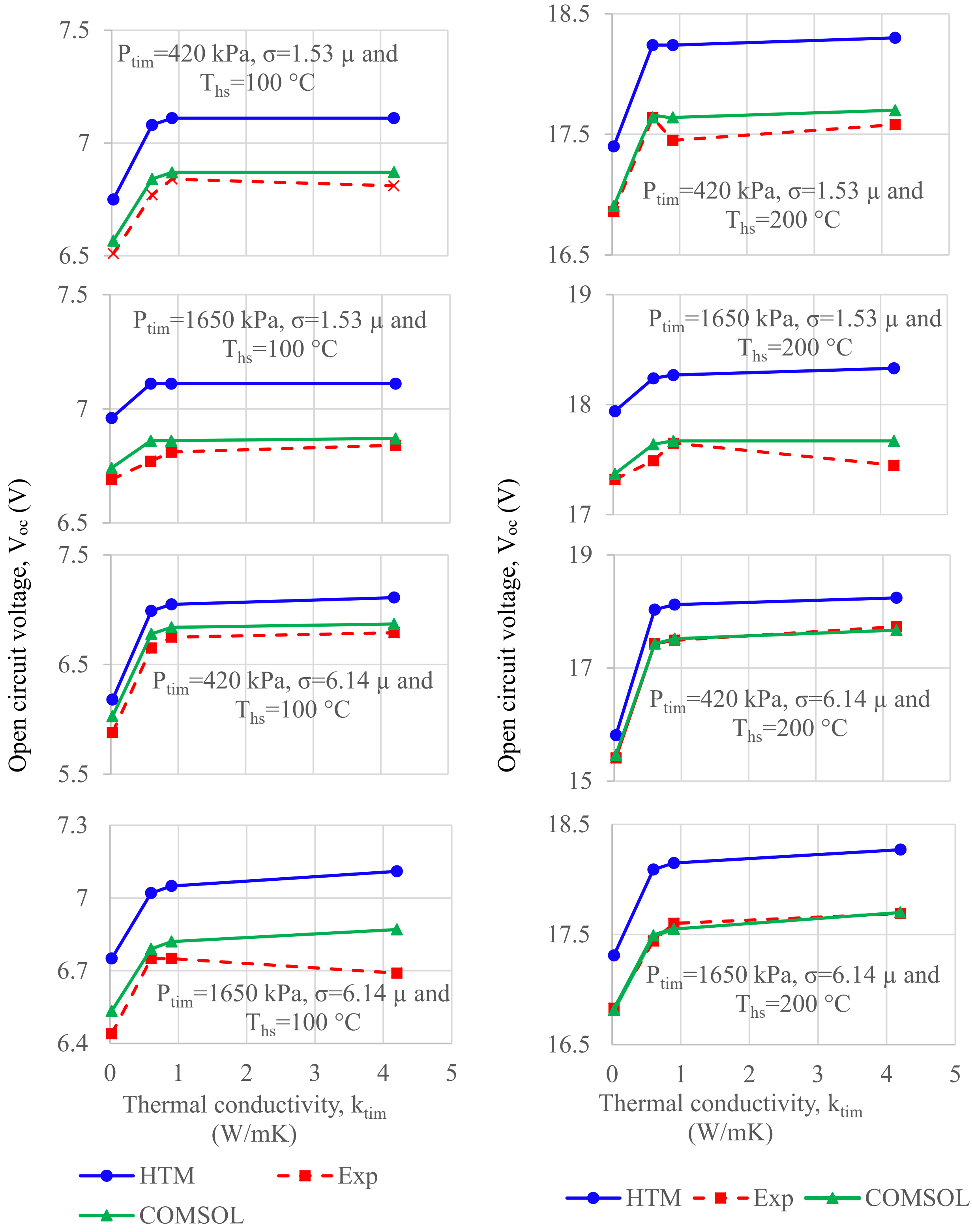

430 **Fig. 12 Influence of thermal conductivity of TIM at open circuit condition**

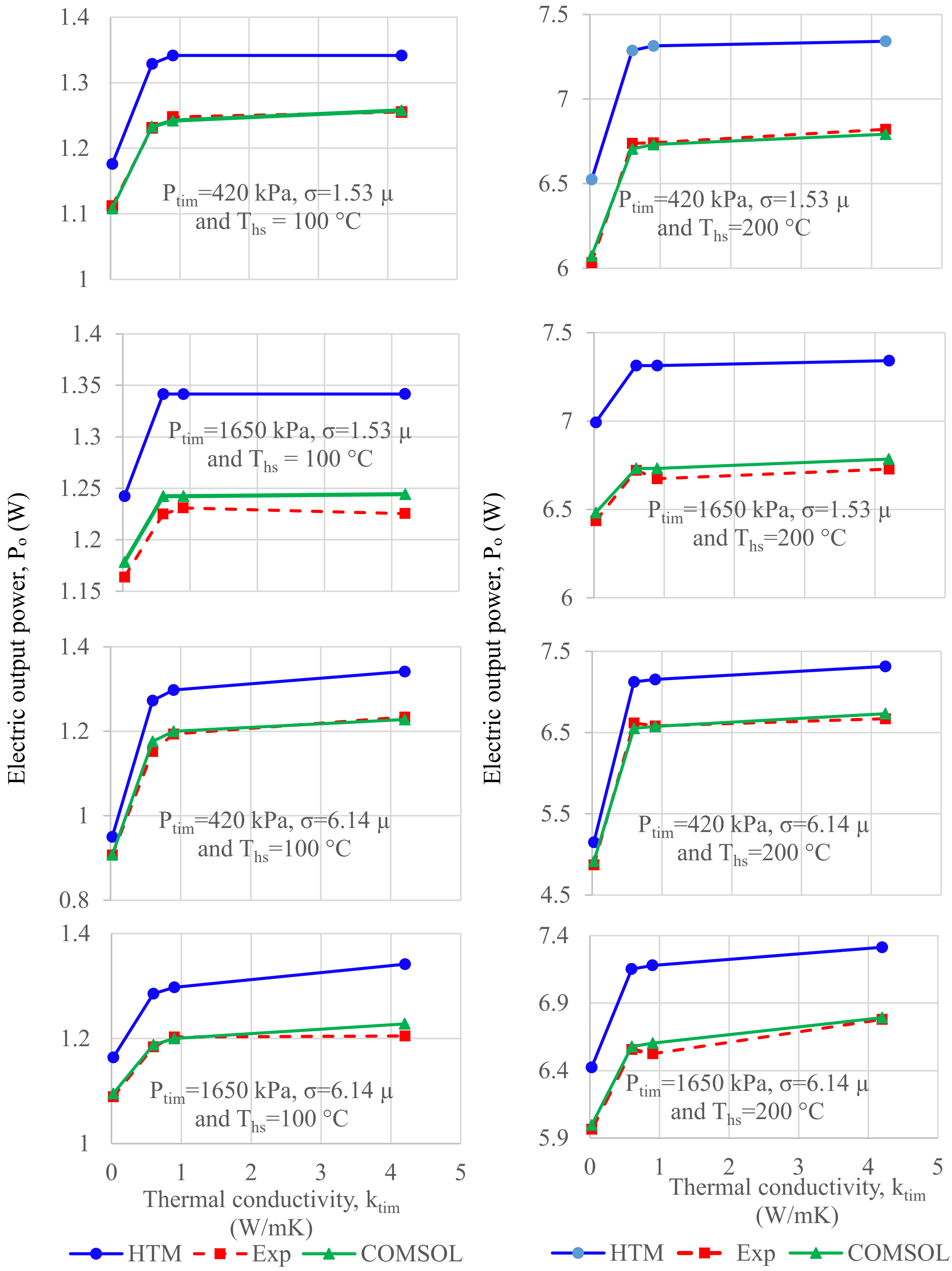

431 **Fig. 13 Influence of thermal conductivity of TIM at closed circuit condition**

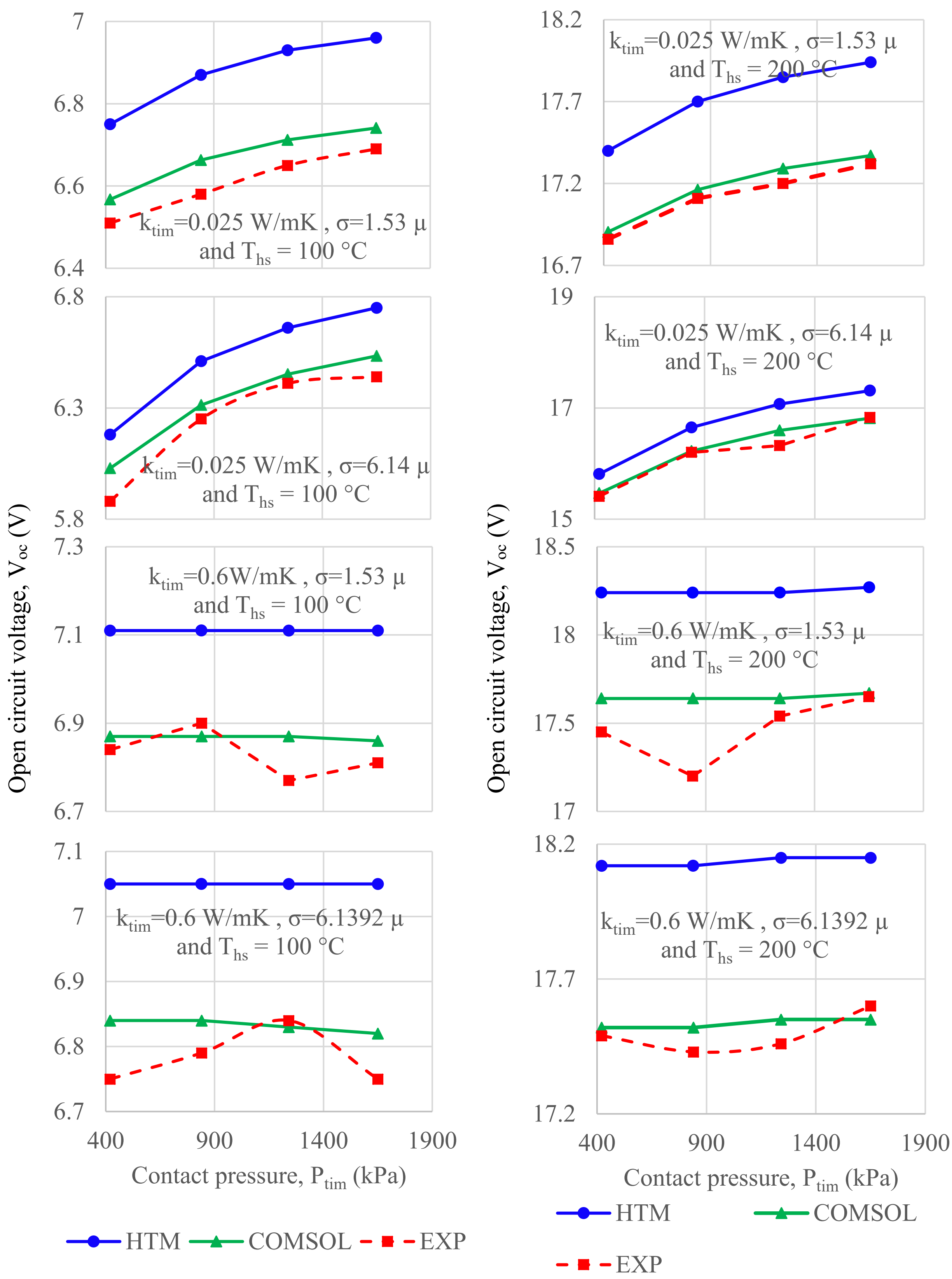

432 **Fig. 14 Influence of contact pressure and TIM at open circuit condition**

433

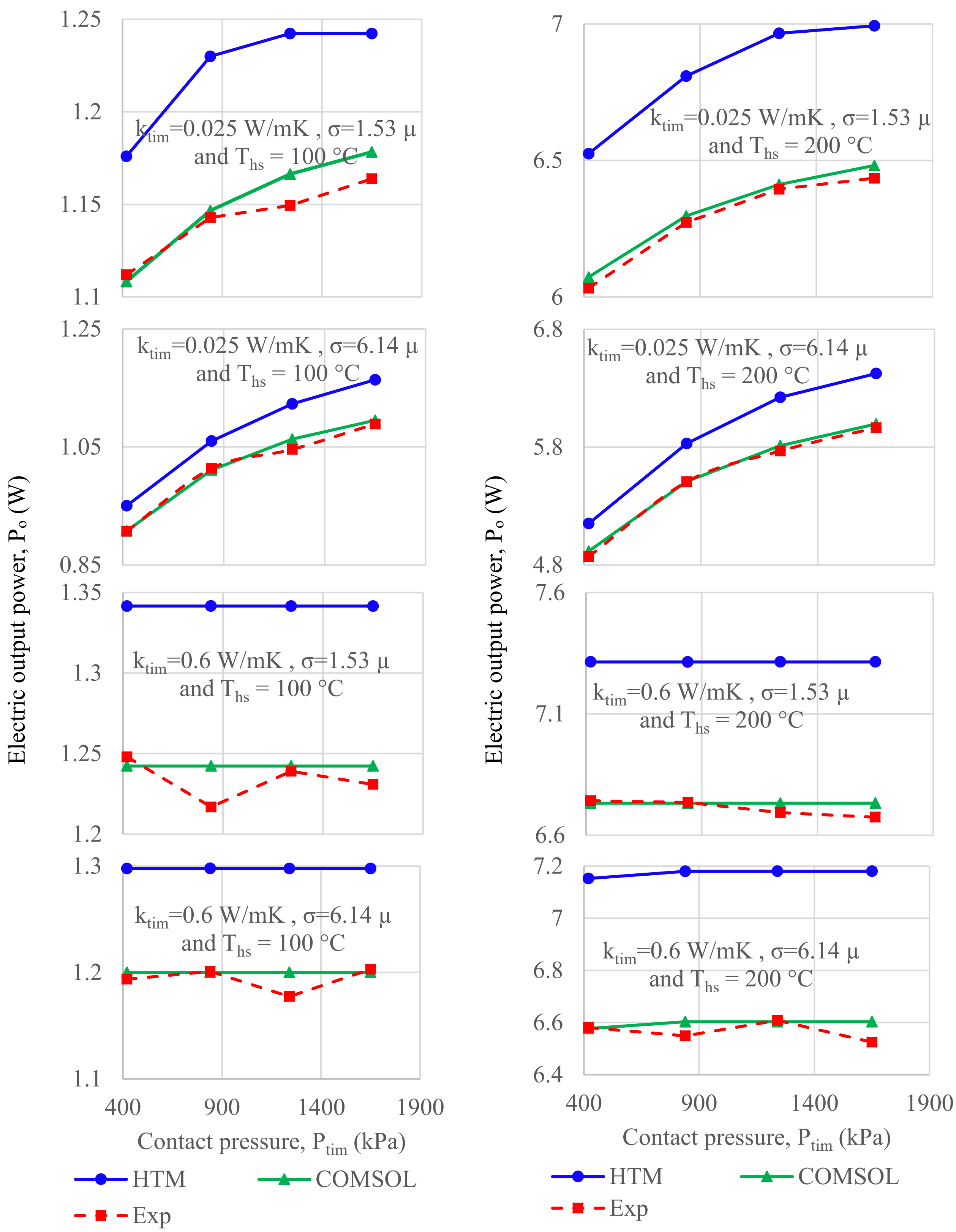

434 **Fig. 15 Influence of contact pressure and TIM at closed circuit condition**

435

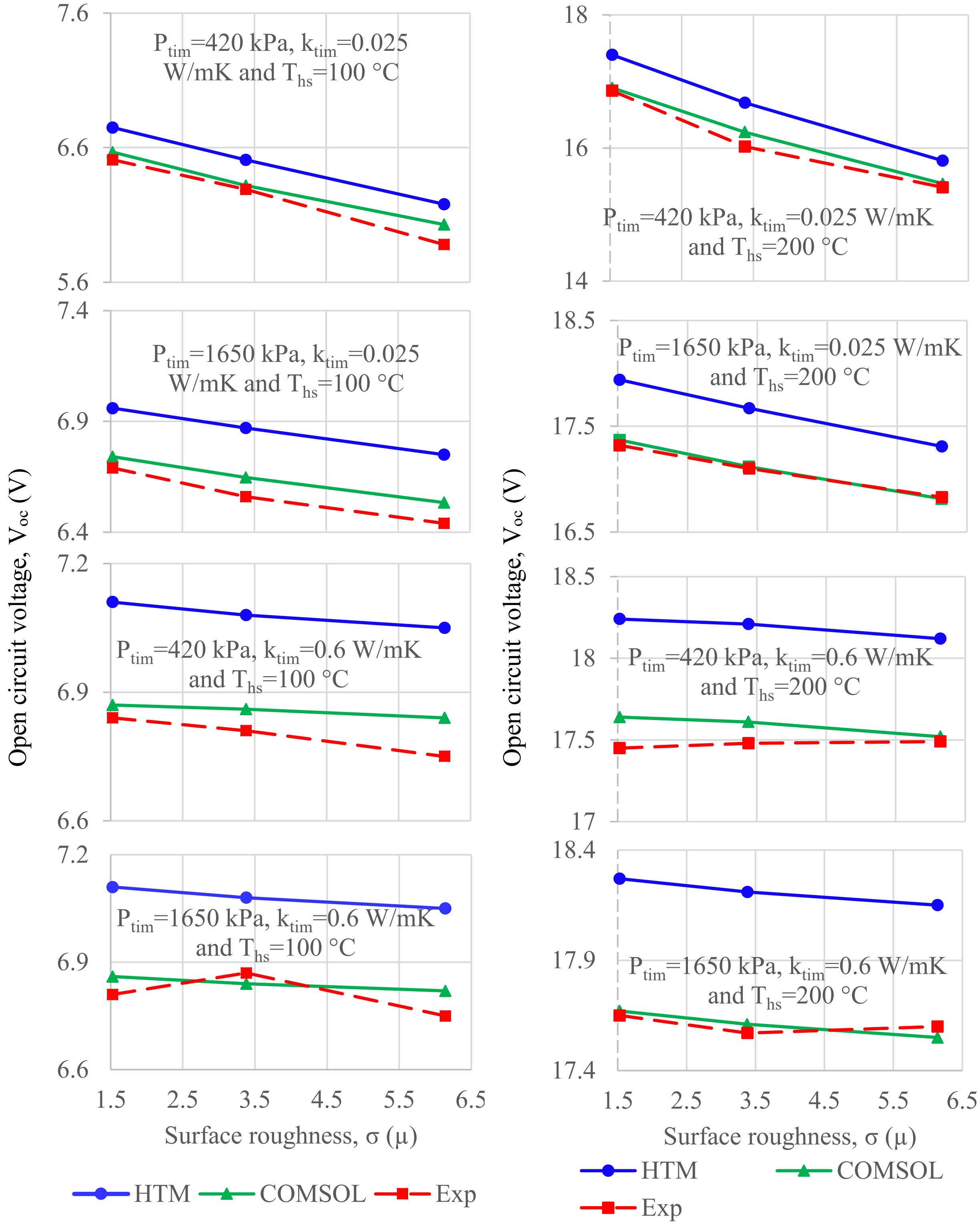

436 **Fig. 16 Influence of surface roughness and TIM at open circuit condition**

437

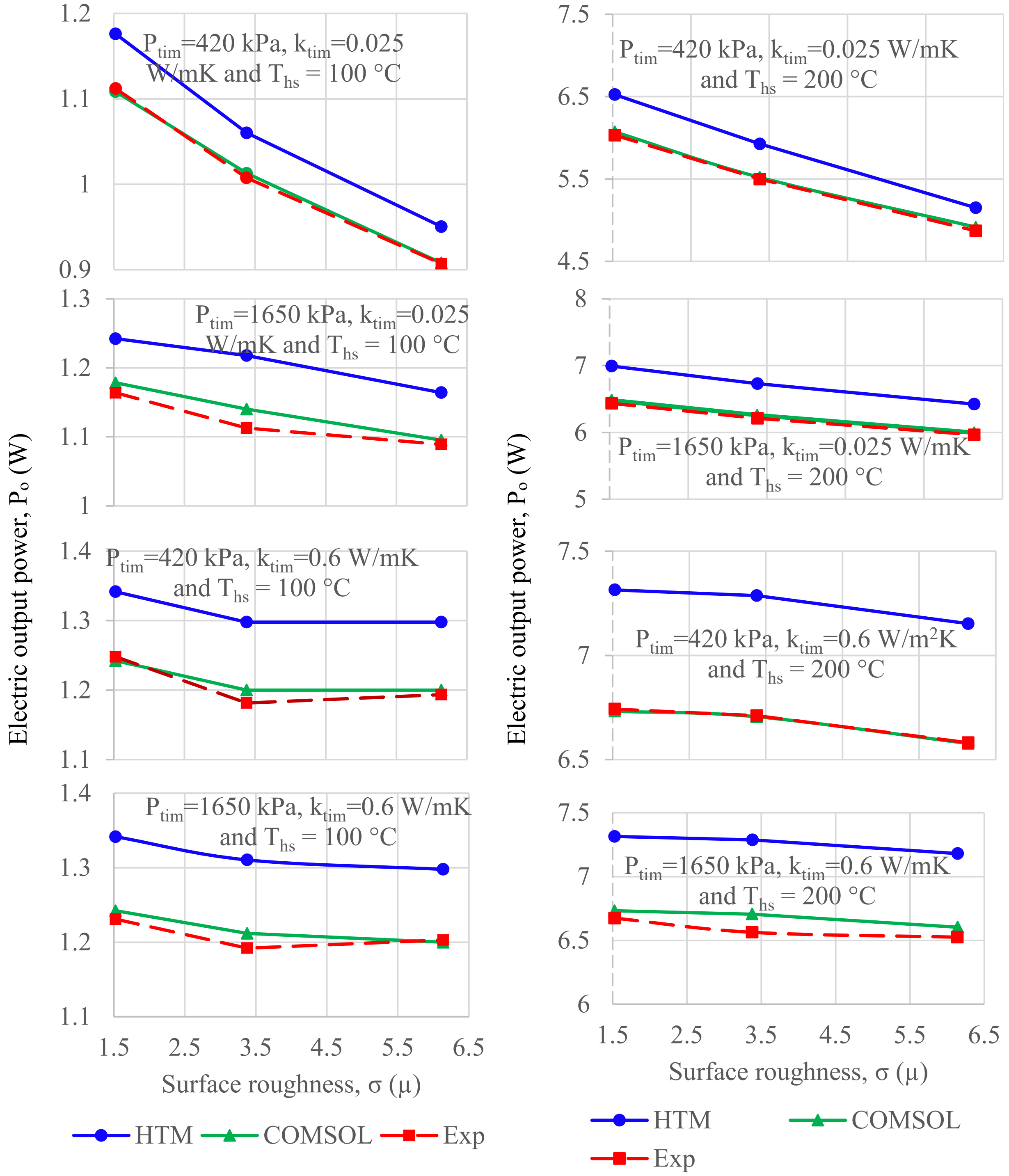

438 **Fig. 17 Influence of surface roughness and TIM at closed circuit condition**

439

440

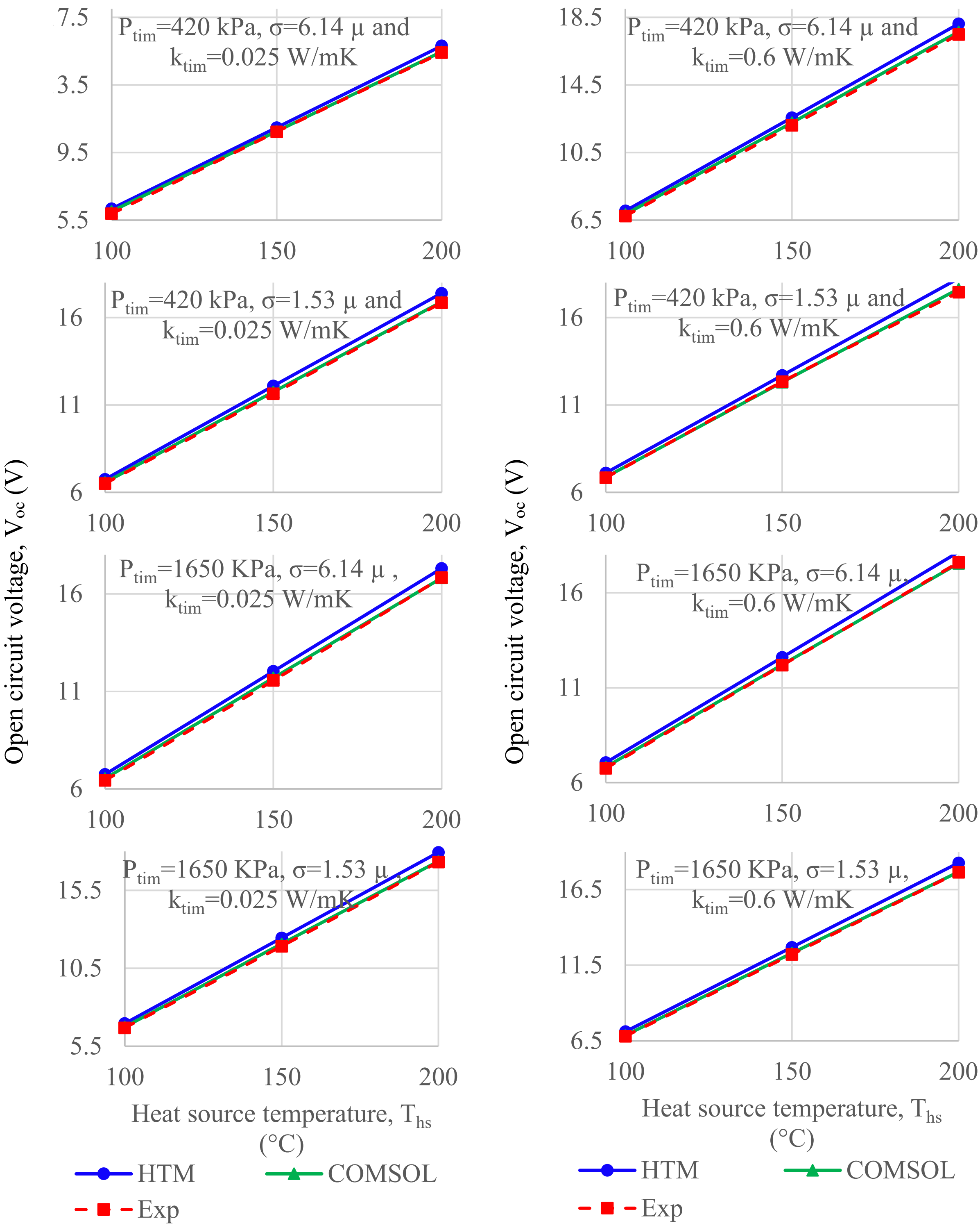

Fig. 18 Influence of heat source temperature at open circuit condition

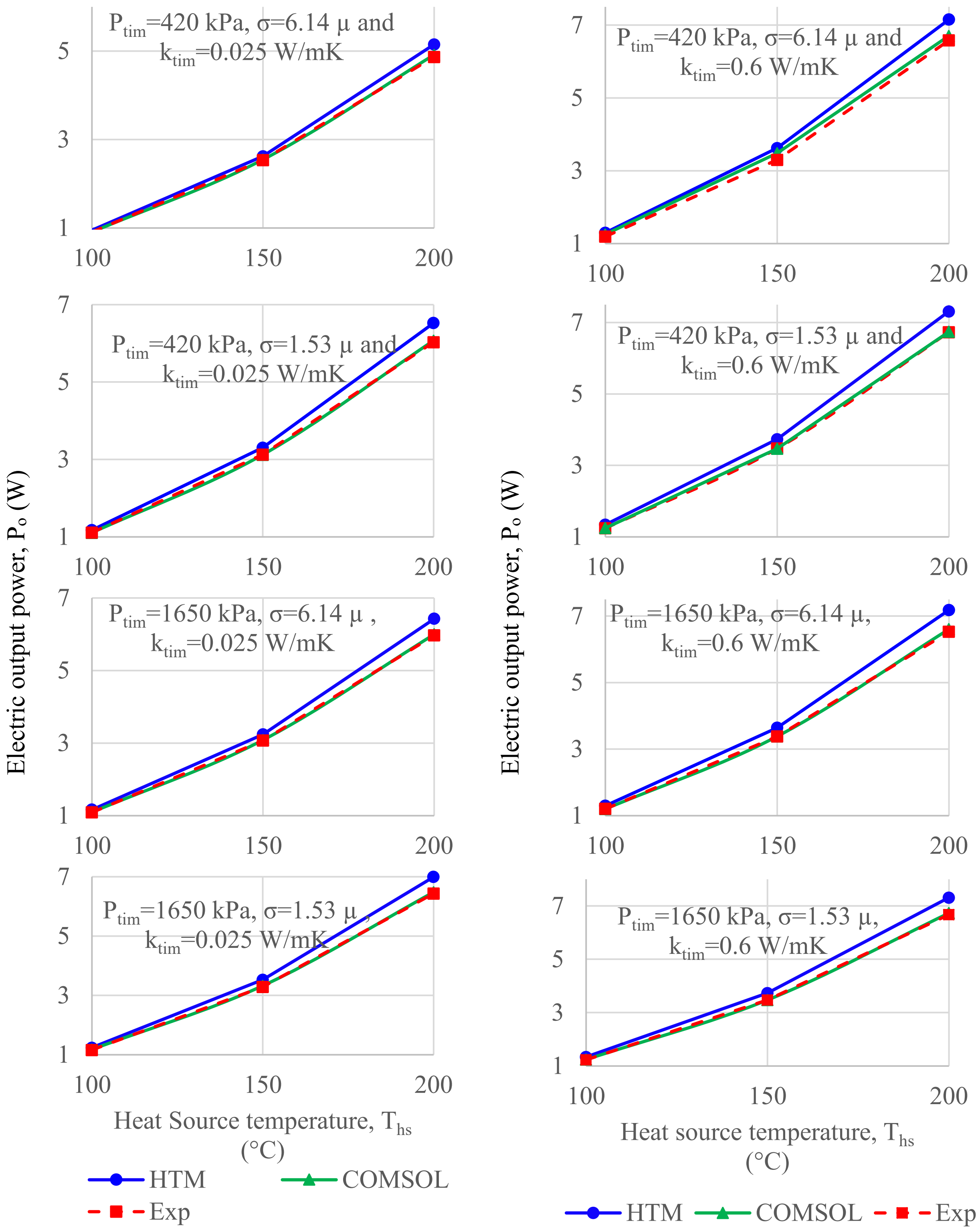

Fig. 19 Influence of heat source temperature at closed circuit condition

5 Conclusions

Experiments were carried out with different Thermal Interface Materials (TIM) of different thermal conductivities at varying conditions of contact pressure, surface roughness and heat source temperature. Mathematical Heat Transfer Model and numerical model using COMSOL™ Multiphysics were developed and validated with the experimental results. The impacts of thermal conductivity, contact pressure, surface roughness and heat source temperature on the thermal performance of TIM and in turn the performance of TEG were evaluated.

The following are the observations:

1. A TIM material having a thermal conductivity of 0.6 W/mK was found to be the best; increasing the thermal conductivities to 0.9 and 4.2 W/mK did not have appreciable increase in voltage and power output from TEG. Hence, use of expensive TIMs comprising MWCNT and Cu NPs may not be required.
2. Increase in contact pressure improves voltage and power outputs at all conditions for a case when no TIM (only entrapped air) is used. It does not have any effect at any condition for TIMs having higher thermal conductivities of 0.6, 0.9 and 4.2 W/mK.
3. Increase in surface roughness decreases the voltage and power output at all conditions for a case when no TIM (only entrapped air) is used. Surface roughness effect is insignificant for TIMs having higher thermal conductivities of 0.6, 0.9 and 4.2 W/mK.
4. Increase in source temperature increases the voltage and power output irrespective of the TIM used. For the same source temperature, the outputs increase with increase in thermal conductivity of TIM.
5. The trends of the outputs of both COMSOL™ and Heat Transfer Models (HTM) were in line with the observations of experiments. However, the outputs of COMSOL™ Multiphysics model had a closer agreement with experimental observation than that of mathematical heat transfer model.

References:

[1] K. Yin, X. Su, Y. Yan, H. Tang, M.G. Kanatzidis, C. Uher, X. Tang, Morphology modulation of SiC nano-additives for mechanical robust high thermoelectric performance Mg 2 Si 1− x Sn x/SiC nano-composites, Scr. Mater. 126 (2017) 1-5. https://doi.org/10.1016/j.scriptamat.2016.08.010.

[2] V.T. Tran, J. Saint-Martin, P. Dollfus, S. Volz, Optimizing the thermoelectric performance of graphene nano-ribbons without degrading the electronic properties, Sci Rep. (2017) 7. 10.1038/s41598-017-02230-0

[3] M. Mohebali, Y. Liu, L. Tayebi, J. S. Krasinski, D. Vashaee, Thermoelectric figure of merit of bulk $FeSi_2$-$Si_{0.8}Ge_{0.2}$ nanocomposite and a comparison with b-$FeSi_2$, Renew. Energ. 74 (2015) 940-947. https://doi.org/10.1016/j.renene.2014.08.059.

[4] Y.J. Kim, L.D. Zhao, M.G. Kanatzidis, D.N. Seidman, Analysis of nano-precipitates in a Na-doped PbTe-SrTe thermoelectric material with a high figure of merit. ACS Appl. Mater. Interfaces. 9 (2017) 21791-7. 10.1021/acsami.7b04098.

[5] J. Wang, B.Y. Zhang, H.J. Kang, Y. Li, X. Yaer, J.F. Li, Q. Tan, S. Zhang, G.H. Fan, C.Y. Liu, L. Miao, Record high thermoelectric performance in bulk SrTiO 3 via nano-scale modulation doping. Nano Energy. 35 (2017) 387-95. https://doi.org/10.1016/j.nanoen.2017.04.003.

[6] Z. Liu, Y. Wang, W. Gao, J. Mao, H. Geng, J. Shuai, W. Cai, J. Sui, Z. Ren The influence of doping sites on achieving higher thermoelectric performance for nanostructured α-MgAgSb. Nano Energy. 31 (2017) 194-200. https://doi.org/10.1016/j.nanoen.2016.11.010.

[7] R. Yue, J. Xu. Poly, (3, 4-ethylenedioxythiophene) as promising organic thermoelectric materials: a mini-review, Synth. Met. 162 (2012) 912-7. https://doi.org/10.1016/j.synthmet.2012.04.005.

[8] K. Koumoto, Y. Wang, R. Zhang, A. Kosuga, R. Funahashi, Oxide thermoelectric materials: a nanostructuring approach, Ann. Rev. Mater. Res. 40 (2010) 463-94.

[9] Y. Yin, B. Tudu, A. Tiwari, Recent advances in oxide thermoelectric materials and modules. Vacuum. 2017 Apr 8. https://doi.org/10.1016/j.vacuum.2017.04.015.

[10] D.M. Rowe, Thermoelectrics handbook macro to nano, 1st ed. Florida, BocaRaton: CRC Press; 2006.

[11] B.V.K. Reddy, M. Barry, J. Li, M.K. Chyu, Thermo-electric-hydraulic performance ofa multistage integrated thermoelectric device, Energy Convers Manage. 77 (2014) 458–68. https://doi.org/10.1016/j.enconman.2013.09.040.

[12] Cheng-Ting Hsu, Gia-Yeh Huang, Hsu-Shen Chu, Ben Yu, Da-Jeng Yao, Experiments and simulations on low-temperature waste heat harvesting system by thermoelectric power generators, Appl. Energy 88 (2011) 1291–1297. https://doi.org/10.1016/j.apenergy.2010.10.005.

[13] B. Orr, A. Akbarzadeh, M. Mochizuki, R. Singh, A review of car waste heat recovery systems utilising thermoelectric generators and heat pipes, Appl. Therm. Eng. 101 (2016) 49. https://doi.org/10.1016/j.applthermaleng.2015.10.081.

[14] R. Ovik, B.D. Long, M.C. Barma, M. Riaz, M.F. Sabri, S.M. Said, R. Saidur A review on nanostructures of high-temperature thermoelectric materials for waste heat recovery, Renew. Sust. Energ. Rev, 64 (2016) 635-59. https://doi.org/10.1016/j.rser.2016.06.035.

[15] I. Sarbu, A. Dorca, A comprehensive review of solar thermoelectric cooling systems. Int. J. Energy Res. 2017. https://doi.org/10.1002/er.3795

[16] P. Huen, W.A. Daoud, Advances in hybrid solar photovoltaic and thermoelectric generators. Renew. Sust. Energ. Rev. 72 (2017) 1295-302. https://doi.org/10.1016/j.rser.2016.10.042.

[17] S. Shaikh, K. Lafdi, E. Silverman, The effect of a CNT interface on the thermal resistance of contacting surfaces, Carbon 45 (2007) 695–703. https://doi.org/10.1016/j.carbon.2006.12.007.

[18] J. Xu, T.S. Fisher, Enhancement of thermal interface materials with carbon nanotube arrays, Int. J. Heat Mass Transfer. 49 (2006) 1658-1666. https://doi.org/10.1016/j.ijheatmasstransfer.2005.09.039.

[19] B.A. Cola, S.L. Hodson, X. Xu, T.S. Fisher, Carbon nanotube array thermal interfaces enhanced with paraffin wax, Proceedings of ASME Summer Heat Conference 2008. doi:10.1115/HT2008-56483.

[20] A. Sarhadi, R. Bjørk, N. Lindeburg, P. Viereck, N. Pryds, A thermoelectric power generating heat exchanger: Part II–Numerical modeling and optimization, Energy Convers Manage. 119 (2016) 481-7. https://doi.org/10.1016/j.enconman.2016.04.052.

[21] D. Astrain, J.G. Vián, A. Martinez, A. Rodríguez, Study of the influence of heat exchangers' thermal resistances on a thermoelectric generation system, Energy. 35 (2010) 602-10. https://doi.org/10.1016/j.energy.2009.10.031.

[22] S. Wang, T. Xie, and H. Xie, Experimental study of the effects of the thermal contact resistance on the performance of thermoelectric generator, Appl. Therm. Eng. 130 (2018) 847-853. https://doi.org/10.1016/j.applthermaleng.2017.11.036.

[23] COMSOL 5.2 User Guide, COMSOL Inc, Burlington, MA, 2015.

[24] M. Yovanovich Spacecraft radiative transfer and temperature control.Ch. Thermal Contact Correlation, Prog. Astronaut. and Aeronaut. AIAA, New York 83 (1982) 83-95.

[25] Zhou, Bahgat G. Sammakia, Bruce White, Peter Borgesen, Cheng Chen, Multiscale modeling of Thermoelectric Generators for conversion performance enhancement, Int. J. Heat Mass Transf 84 (2015) 639-645. https://doi.org/10.1016/j.ijheatmasstransfer.2014.10.068.

[26] M.C. Barma, M. Riaz, R. Saidur, B.D, Long, Estimation of thermoelectric power generation by recovering waste heat from Biomass fired thermal oil heater, Energy Convers Manage. 98 (2015) 303–313. https://doi.org/10.1016/j.enconman.2015.03.103.

Nomenclature

A_a	apparent contact area of joining surfaces (m^2)
A_c	effective heat transfer area on cold side (m^2)
A_{ct}	total cross-sectional area of P-type / N-type elements (m^2)
A_{eff}	fin effective area (m^2)
A_{fb}	surface area of the fin base plate (m^2)
A_h	effective heat transfer area on hot side (m^2)
A_{sp}	surface area of the heat spreader plate (m^2)
b	tunnel width (m)
E	magnetic field (V)
h	combined thermal interface conductance (W/m^2K)
h_c	contact conductance (W/m^2K)
H_c	micro-hardness of softer contact surface of the two surfaces in contact (MPa)
h_{camb}	heat transfer coefficient between fin and ambient (W/m^2K)
H_f	height of the fin (m)
h_g	gap conductance (W/m^2K)
H_l	height of the TEG element (m)
I_o	output current (A)
J	TEG current density (A/m^2)
k	thermal conductivity (W/mK)

K	thermal conductance (W/K)
k_f	thermal conductivity of fin (W/mK)
k_{fb}	thermal conductivity fin base plate (W/mK)
k_s	harmonic mean mean of two contacting surfaces thermal conductivity (W/mK)
k_{sp}	thermal conductivity of the heat spreader plate (W/mK)
k_{tim}	Thermal conductivity of TIM (W/mK)
$k(T)$	thermal conductivity of the P-N couple (W/mK)
L	height of P-type and N-type elements (m)
L_f	length of the fin (m)
L_{fb}	length of the fin base plate (m)
L_{sp}	length of the heat spreader plate (m)
m_s	absolute mean asperity slope
m_i	effective absolute mean asperity slope
n	normal vector to the boundary
N_c	number of couple in TEG (No)
N_f	number of fin (No)
p	perimeter of the fin tip (m)
P_o	electric power output (W)
P_{tim}	contact pressure (MPa)
Q_c	Rate of heat transferred from cold side of TEG (W)
Q_h	heat absorption by TEG (W)
R_c	thermal interface resistance due to contact (m^2K/W)
R_{ci}	combined resistances of TEG cold side interface (m^2K/W)
R_{camb}	ambient thermal resistance (m^2K/W)
R_{fb}	fin base plate thermal resistance (m^2K/W)
R_g	thermal interface resistance due to gap (m^2K/W)
R_{hi}	combined resistances of TEG hot side interface (m^2K/W)
R_L	external load resistance (Ω)
R_{sp}	thermal resistance of heat spreader plate (m^2K/W)
R_{teg}	TEG internal resistance (Ω)
T_a	ambient temperature (K)
t_f	thickness of the fin (m)
t_{fb}	thickness of the fin base plate (m)
T_{hs}	heat source surface temperature (K)

T	temperature (K)
T_h	TEG hot side temperature (K)
T_c	TEG cold temperature (K)
t_{sp}	thickness of the heat spreader plate (m)
U_c	overall heat transfer coefficient on hot side (W /m^2K)
U_h	overall heat transfer coefficient on hot side (W /m^2K)
V_o	TEG output voltage (V)
V_{oc}	TEG open circuit voltage (V)
V_w	wind velocity (m/s)
W_{fb}	width of the fin base plate (m)
W_{sp}	width of the heat spreader plate (m)
Y	layer thickness of the TIM (m)
$[k]$	thermal conductivity of TEG leg matrix (W/mK)

Greek symbol

α	Seebeck coefficient of TEG module (V/K)
$[\alpha]$	Seebeck coefficient of TEG leg matrix (V/K)
α_a and β	gas parameters
$\alpha(T)$	Seebeck coefficient of the P-N couple (V/K)
$\wedge$	molecular free path (m)
ϕ	electric scalar potential (V)
η_f	fin efficiency (%)
ρ	electrical resistivity (Ωm)
$\rho(T)$	electrical resistivity of the P-N couple (Ωm)
$[\Pi]$	Peltier coefficient of TEG leg matrix which depends on $T[\alpha]$ (W/A)
σ	effective RMS surface roughness (m)
σ_{Al}	Surface roughness of base plate material surface (m)
σ_e	electrical conductivity of TEG leg matrix (S/m)
$[\sigma_e]$	electrical conductivity of TEG leg matrix (S/m)
σ_i	effective absolute surface roughness (μ)
σ_{teg}	Surface roughness of TEG module surface (m)

Subscript

d	downside of the slit
u	upside of the slit